Mathematical Models and Methods in Applied Sciences
Vol. 32, No. 12 (2022) 2529–2550

DOI: 10.1142/S0218202522500609

Isogeometric large-eddy simulations of turbulent particle-laden flows

Qiming Zhu*, Minjiang Zhu† and Jinhui Yan‡

Department of Civil and Environmental Engineering,
University of Illinois Urbana-Champaign,
205 N Mathews Ave, Urbana, IL 61801, USA
**qiming2@illinois.edu*
†mz51@illinois.edu
‡yjh@illinois.edu

Received 14 July 2022
Revised 26 August 2022
Accepted 3 October 2022
Published 3 December 2022
Communicated by K. Takizawa

In recent years, isogeometric analysis (IGA) has attracted significant attention from the computational mechanics community due to its ability to integrate design and analysis. Besides, IGA is also a higher-order discretization technique for solving partial differential equations, showing high approximation capability per degree of freedom. In this paper, we extend the application realm of IGA to particle-laden flows based on Eulerian–Eulerian description that couples Navier–Stokes equations with a density transport equation through a Boussinesq approximation. The coupled systems are solved by using quadratic non-uniform rational B-spline (NURBS) functions and a recently developed residual-based variational multiscale (VMS) formulation, which introduces coupling between the fine velocity scales and density equation residuals. We deploy the proposed approach to perform large-eddy simulations (LES) of dilute particle-laden flows over a flat surface at Reynolds number = 10,000. We compare the simulation results against direct numerical simulation (DNS) results from the literature. We find that combining VMS and IGA, the proposed approach enables accurate prediction of a wide range of flow/particle statistics with a relatively lower mesh resolution.

Keywords: Isogeometric analysis; large-eddy simulation; particle-laden flows.

AMS Subject Classification: 22E46, 53C35, 57S20

1. Introduction

Particle-laden flows are ubiquitous in many natural and engineering systems. Representative examples include volcano eruptions, oil spills, snow avalanches, and

‡Corresponding author.

powder dynamics in additive manufacturing processes. In recent years, computational fluid dynamics has been playing a critical role in revealing the fundamental physics of particle-laden flows.[37, 38, 72, 115] One critical issue of simulations of particle-laden flows is how to handle the particle motions in the carrying fluid. There are two common approaches.[113] The first one is the Eulerian–Lagrangian approach, in which the carrying fluid is modeled by an Eulerian description, while the particle motion is explicitly tracked by a Lagrangian description (e.g. discrete element method). In particular, early work in the late 1990s[48–51] applied Deforming-Spatial-Domain/Stabilized Space–Time[110] to simulate fluid–particle interactions in the sedimentation process of spherical particles in a liquid tube. The approach, now called as Space–Time SUPS (ST–SUPS) because of its stabilization components Streamline-Upwind/Petrov–Galerkin (SUPG)[29] and Pressure-Stabilizing/Petrov–Galerkin (PSPG),[110] is an effective technique for a wide range of flow problems involving moving boundaries and interfaces. For the fluid–particle interaction, the ST–SUPS in these referred papers uses moving meshes to explicitly represent the falling particles, leading to exceptional accuracy of particle dynamics and their interaction with the surrounding flows. However, a problem with the Eulerian–Lagrangian approach is that it may incur a prohibitive computational cost once the number of particles becomes large. In particular, in some geotechnical or additive manufacturing applications, the number of particles can exceed 10^5. This issue confines the applications of the Eulerian–Lagrangian approach to particle-laden flows with large particle sizes and high particle mass fractions.[31, 39, 68, 85, 114]

The second approach is the Eulerian–Eulerian approach, in which both the carrying fluid and the particles are handled in Eulerian description. This approach is suitable for particle-laden flows with low particle mass fractions. In this approach, the particle behaves essentially like a second fluid. Although the Eulerian–Eulerian approach possesses lower accuracy since particles are not handled explicitly, its low computational cost makes this approach popular in many problems with a large number of particles and low particle mass fractions[55, 69, 81].

The past 17 years have witnessed the boom of applications of isogeometric analysis (IGA) in various engineering fields since its inception. IGA, originally proposed in,[45] aims to automate the design-through-analysis pipeline by directly employing the spline functions that describe computer-aided design (CAD) models in engineering analysis. From the perspective of pure analysis, IGA possesses higher accuracy than the standard finite element-based counterpart, attributed to the higher approximation ability of smoother spline basis functions. This superior approximation property enables IGA to tackle mechanics problems involving higher-order differential operators and achieve high accuracy with fewer degrees of freedom.

Although successful applications of IGA to many fluid, solid, and structural mechanics problems can be found in the literature,[1–3, 7, 10–14, 16, 19, 20, 26–28, 40–42, 53, 56, 62, 65, 70, 71, 78, 101–106, 109, 112, 121, 122] its application to particle-laden flows hasn't been explored yet. This paper presents a numerical formulation by combining the IGA discretization with a modified residual-based variational multiscale (RBVMS) formulation to simulate high Reynolds number particle-laden flows under an Eulerian–Eulerian description. The formulation employs a two-way coupled Navier–Stokes and convection–diffusion equations through the Boussinesq approximation. Taking advantage of IGA's high approximation accuracy and VMS's capability in capturing multiscale phenomena, the formulation achieves effective large-eddy simulations of turbulent particle-laden flows. Compared with the original RBVMS in,[9] the modified RBVMS used in this paper, which couples the fine-scale velocity and density equation residuals, shows enhanced performance in capturing critical statistics in coupled Eulerian–Eulerian systems (e.g. density or temperature-stratified turbulent flows[120]). We utilize the VMS–IGA method to simulate particle-laden flows in the lock-exchange configuration with a horizontal bottom surface. We compare the VMS–IGA results with available DNS results to show how the higher smooth IGA basis functions, combined with RBVMS, obtain accurate predictions with a mesh with lower resolution.

This paper is arranged as follows. In Sec. 2, the governing equations of particle-laden flows in the Eulerian–Eulerian description are presented. The basics of IGA and RBVMS are briefly given in Sec. 3. We present the computational setup in Sec. 4. The simulation results are presented and discussed in Sec. 5. Section 6 summarizes the conclusions.

2. Governing Equations

The Eulerian–Eulerian description adopted in this paper uses a Boussinesq approximation, assuming the particle diameter and the particle Stokes number are sufficiently small in the flow. The density is treated as constant in the momentum equations augmented with a body forcing term. Instead of tracking individual particles in a Lagrangian fashion, a convection–diffusion equation is utilized to model the concentration of particles. With the above assumptions, the governing equations of particle-laden flows consist of momentum conservation, mass conservation, and a scalar transport equation. The dimensionless form of governing equations is given as follows:

$$\frac{\partial \boldsymbol{u}}{\partial t} + \boldsymbol{u} \cdot \nabla \boldsymbol{u} + \nabla p - \frac{1}{\mathrm{Re}} \nabla^2 \boldsymbol{u} - \rho \boldsymbol{e}_g = 0, \tag{2.1}$$

$$\nabla \cdot \boldsymbol{u} = 0, \tag{2.2}$$

$$\frac{\partial \rho}{\partial t} + \boldsymbol{u}_p \cdot \nabla \rho - \frac{1}{\mathrm{S_c}\,\mathrm{Re}} \nabla^2 \rho = 0, \tag{2.3}$$

where t, $\boldsymbol{u}$, $\boldsymbol{u}_p$, p, and ρ are the dimensionless time, fluid velocity, particle convective velocity, pressure, and density, respectively. They are defined based on dimensional time $\tilde{t}$, fluid velocity $\tilde{\boldsymbol{u}}$, particle convective velocity $\tilde{\boldsymbol{u}}_p$, pressure $\tilde{p}$, and density $\tilde{\rho}$ as follows:

$$\boldsymbol{u} = \frac{\tilde{\boldsymbol{u}}}{\tilde{u}_b}, \quad \boldsymbol{u}_p = \frac{\tilde{\boldsymbol{u}}_p}{\tilde{u}_b}, \quad p = \frac{\tilde{p}}{\tilde{\rho}_c \tilde{u}_b^2}, \quad \rho = \frac{\tilde{\rho} - \tilde{\rho}_l}{\tilde{\rho}_h - \tilde{\rho}_l}, \quad t = \frac{2\tilde{t}\tilde{u}_b}{\tilde{H}}, \tag{2.4}$$

where $\tilde{u}_b = \sqrt{\frac{\tilde{g}'\tilde{H}}{2}}$ is the buoyancy velocity, $\tilde{g}' = \tilde{g}\frac{\tilde{\rho}_h - \tilde{\rho}_l}{\tilde{\rho}_c}$ is the reduced gravitational acceleration magnitude, in which $\tilde{\rho}_c$ represents the carrier fluid density, $\tilde{g}$ is the gravity acceleration magnitude, and $\tilde{H}$ is the height of the domain. $\tilde{\rho}_h$ and $\tilde{\rho}_l$ are densities of heavy and light fluids, respectively. $\tilde{\boldsymbol{u}}_p$ is the dimensional particle convective velocity, which is obtained by superimposing the fluid velocity $\tilde{\boldsymbol{u}}$ and particle settling velocity $\tilde{u}_s$

$$\tilde{\boldsymbol{u}}_p = \tilde{\boldsymbol{u}} + \tilde{u}_s \boldsymbol{e}_g, \tag{2.5}$$

where $\boldsymbol{e}_g$ is the unit vector in the gravity direction. The settling velocity $\tilde{u}_s$ is given by Stokes law as

$$\tilde{u}_s = \frac{(\tilde{\rho}_p - \tilde{\rho}_c)\tilde{g}\tilde{d}_p^2}{18\tilde{\mu}}, \tag{2.6}$$

where $\tilde{\mu}$ is the dynamic viscosity, $\tilde{\rho}_p$ is the particle density, and $\tilde{d}_p$ is the particle diameter. Here, we also have dimensionless setting velocity as $u_s = \frac{\tilde{u}_s}{\tilde{u}_b}$.

The particle-laden flows governed by Eqs. (2.1)–(2.3) can be characterized by Reynolds number Re and Schmidt number $\mathrm{S_c}$, which are defined as

$$\mathrm{Re} = \frac{\tilde{u}_b\tilde{H}}{2\tilde{\nu}}, \tag{2.7}$$

$$\mathrm{S_c} = \frac{\tilde{\nu}}{\tilde{\alpha}}, \tag{2.8}$$

where $\tilde{\nu}$ is the kinematic viscosity and $\tilde{\alpha}$ is the molecular diffusivity.

3. Numerical Formulation

3.1. *Isogeometric analysis*

The basics of IGA are presented in this section. IGA employs B-splines and Non-uniform rational B-splines (NURBS) that are used in CAD descriptions of geometric models as the basis functions in engineering analysis. These basis functions have higher-order continuity and other better properties than Lagrangian polynomials.

B-splines can be expressed by a linear combination of n basis functions of order p and the associated n control points. The functions are defined upon a knot vector, a non-decreasing sequence in parametric space denoted by $\{\xi_1, \xi_2, \ldots, \xi_{n+p-1}\}$, where ξ_i is the i_{th} knot, n is the number of B-spline basis functions, and p is the polynomial order. The interval $[\xi_i, \xi_{i+p+1}]$ is called a knot span. A B-spline basis is C_∞-continuous inside a knot span and C_{p-m}-continuous at knots with multiplicity $m \leq p$. The construction of higher-order B-spline functions $N_{i,p}$ is based on the Cox-de Boor recursion process, starting with piecewise-constant functions $(p = 0)$ on each knot span, namely,

$$N_{i,0}(\xi) = \begin{cases} 1 & \text{if } \xi_i < \xi \leq \xi_{i+1}, \\ 0 & \text{otherwise.} \end{cases} \tag{3.1}$$

For $p > 0$, the Cox-de Boor recursion process leads to

$$N_{i,p}(\xi) = \frac{\xi - \xi_i}{\xi_{i+p} - \xi_i} N_{i,p-1}(\xi) + \frac{\xi_{i+p+1} - \xi}{\xi_{i+p+1} - \xi_{i+1}} N_{i+1,p-1}(\xi). \tag{3.2}$$

NURBS are projections of B-splines from R^{d+1} to R^d, leading to piece-wise rational functions. For each B-spline basis function, its NURBS counterpart $R_{i,p}$ is given as

$$R_{i,p}(\xi) = \frac{N_{i,p}(\xi) w_i}{\sum_{\hat{i}=1}^{n} N_{\hat{i},p}(\xi) w_{\hat{i}}}, \tag{3.3}$$

where $w_{\hat{i}}$ is a positive weight for the $\hat{i}_{\text{th}}$ B-spline function. NURBS basis functions in higher dimensions, such as 3D, are defined by introducing knot vectors in every dimension and employing a tensor-product construction as

$$R_{i,j,k}^{p,q,r} = \frac{N_{i,p}(\xi) M_{j,q}(\eta) L_{k,r}(\zeta)}{\sum_{\hat{i}=1}^{n} \sum_{\hat{j}=1}^{m} \sum_{\hat{k}=1}^{l} N_{\hat{i},p}(\xi) M_{\hat{j},q}(\eta) L_{\hat{k},r}(\zeta) w_{\hat{i}\hat{j}\hat{k}}}. \tag{3.4}$$

NURBS can represents curves, surfaces, and volumes. A NURBS curve $\boldsymbol{C}(\xi)$ is obtained by taking a linear combination of univariate NURBS basis functions from Eq. (3.3) and control points coordinates $\boldsymbol{B}_i$ as

$$\boldsymbol{C}(\xi) = \sum_{i=1}^{n} N_{i,p}(\xi) \boldsymbol{B}_i. \tag{3.5}$$

Similarly, a NURBS volume patch $\boldsymbol{V}(\xi, \eta, \zeta)$ is constructed analogously as

$$\boldsymbol{V}(\xi, \eta, \zeta) = \sum_{i=1}^{n} \sum_{j=1}^{m} \sum_{k=1}^{l} R_{i,j,k}^{p,q,r}(\xi, \eta, \zeta) \boldsymbol{B}_{i,j,k}. \tag{3.6}$$

3.2. *Residual-based variational multiscale formulation*

We employ a RBMVS formulation to solve the coupled Navier–Stokes and density equations. The details are briefly presented as follows. Let V denote the set of discrete trial functions for the velocity, pressure, and density unknowns $\{\boldsymbol{u}, p, \rho\}$ and W denote linear momentum, continuity, and density equations $\{\boldsymbol{w}, q, \eta\}$. The semi-discrete RBVMS formulation is stated as: Find $\{\boldsymbol{u}, p, \rho\} \in V$, such that $\forall \{\boldsymbol{w}, q, \eta\} \in W$,

$$\mathcal{B}_G(\{\boldsymbol{w}, q, \eta\}, \{\boldsymbol{u}, p, \rho\}) + \mathcal{B}_V(\{\boldsymbol{w}, q, \eta\}, \{\boldsymbol{u}, p, \rho\}) = \mathcal{F}(\{\boldsymbol{w}, q, \eta\}), \tag{3.7}$$

where B_G and B_V are the Galerkin formulation of the coupled Navier–Stokes and density equations and fine-scale terms stemming from RBVMS. They are defined as

$$\begin{aligned} \mathcal{B}_G(\{\boldsymbol{w}, q, \eta\}, \{\boldsymbol{u}, p, \rho\}) = {} & \left(\boldsymbol{w}, \frac{\partial \boldsymbol{u}}{\partial t}\right)_\Omega + (\boldsymbol{w}, \boldsymbol{u} \cdot \nabla \boldsymbol{u})_\Omega - (\boldsymbol{w}, \rho \boldsymbol{e}_g)_\Omega - (\nabla \boldsymbol{w}, p\boldsymbol{I})_\Omega \\ & + \left(\nabla \boldsymbol{w}, \frac{1}{\mathrm{Re}} \nabla \boldsymbol{u}\right)_\Omega + (q, \nabla \cdot \boldsymbol{u})_\Omega + \left(\eta, \frac{\partial \rho}{\partial t}\right)_\Omega \\ & + (\eta, \boldsymbol{u}_p \cdot \nabla \rho)_\Omega + \left(\nabla \eta, \frac{1}{\mathrm{S_c}\,\mathrm{Re}} \nabla \rho\right)_\Omega \end{aligned} \tag{3.8}$$

and

$$\begin{aligned}\mathcal{B}_V(\{\boldsymbol{u},p,\rho\},\{\boldsymbol{w},q,\eta\}) = &-(\boldsymbol{u}\cdot\nabla\boldsymbol{w}+\nabla q,\boldsymbol{u}')_\Omega + (\boldsymbol{w},\boldsymbol{u}'\cdot\nabla\boldsymbol{u})_\Omega \\ &-(\nabla\boldsymbol{w},\boldsymbol{u}'\otimes\boldsymbol{u}')_\Omega - (\nabla\cdot\boldsymbol{w},p')_\Omega \\ &-(\boldsymbol{u}\cdot\nabla\eta,\rho')_\Omega \end{aligned} \tag{3.9}$$

where $(\ ,\ )_A$ represents the L_2 inner product over domain A.

$F(\{\boldsymbol{w},q,\eta\})$ is defined as

$$\mathcal{F}(\{\boldsymbol{w},q,\eta\}) = (\boldsymbol{w},\boldsymbol{h})_{\Gamma_f} + (\eta,Q)_{\Gamma_d} \tag{3.10}$$

where $\boldsymbol{h}$ is the traction on Γ_f, and Q is the density flux on Γ_d.

In Eq. (3.9), $\boldsymbol{u}', p'$, and ρ' are the fine-scale velocity, pressure, and density fields, which are modeled based on the residuals of the strong form momentum, continuity, and density equations, and given by

$$\begin{bmatrix}\boldsymbol{u}'\\ \rho'\\ p'\end{bmatrix} = -\begin{bmatrix}\boldsymbol{\tau}_{4\times4} & \\ & \tau_c\end{bmatrix}\begin{bmatrix}\boldsymbol{r_m}\\ r_\rho\\ r_c\end{bmatrix}, \tag{3.11}$$

where $\boldsymbol{r_m}$, r_ρ, and r_c are the residuals of the momentum, density and continuity equations, respectively, given as

$$\boldsymbol{r}_m = \frac{\partial\boldsymbol{u}}{\partial t} + \boldsymbol{u}\cdot\nabla\boldsymbol{u} + \nabla p - \frac{1}{\mathrm{Re}}\nabla^2\boldsymbol{u} - \rho\boldsymbol{e}_g, \tag{3.12}$$

$$r_c = \nabla\cdot\boldsymbol{u}, \tag{3.13}$$

$$r_\rho = \frac{\partial\rho}{\partial t} + \boldsymbol{u}_p\cdot\nabla\rho - \frac{1}{\mathrm{S_c\ Re}}\nabla^2\rho \tag{3.14}$$

$[\boldsymbol{\tau}]_{4\times4}$ and τ_c and are the fine-scale parameters. For more discussions, readers are referred to the work in.[32, 115, 120] Here, we skip the derivation and directly present their definitions. $[\boldsymbol{\tau}]_{4\times4}$ is defined as

$$[\boldsymbol{\tau}]_{4\times4} = \begin{bmatrix}\tau_m & & & \\ & \tau_m & & \\ & & \tau_m & \tau_{u\rho} \\ & & & \tau_\rho\end{bmatrix}, \tag{3.15}$$

where τ_m, τ_ρ, and $\tau_{u\rho}$ are defined as

$$\tau_m = \left(\frac{4}{\Delta t^2} + \boldsymbol{u}\cdot\boldsymbol{G}\boldsymbol{u} + \frac{C_I}{\mathrm{Re}^2}\boldsymbol{G}:\boldsymbol{G}\right)^{-1/2}, \tag{3.16}$$

$$\tau_\rho = \left(\frac{4}{\Delta t^2} + \boldsymbol{u}_p\cdot\boldsymbol{G}\boldsymbol{u}_p + \frac{C_I}{\mathrm{S_c^2\ Re^2}}\boldsymbol{G}:\boldsymbol{G}\right)^{-1/2}, \tag{3.17}$$

$$\tau_{u\rho} = -\frac{4}{\Delta t(\tau_m^{-1}\tau_\rho^{-2} + \tau_m^{-2}\tau_\rho^{-1})}, \tag{3.18}$$

where Δt is the time step, $\boldsymbol{G}$ is the element mesh metric tensor, given by $\boldsymbol{G} = \frac{\partial \boldsymbol{\xi}}{\partial \boldsymbol{x}}(\frac{\partial \boldsymbol{\xi}}{\partial \boldsymbol{x}})^T$, where $\frac{\partial \boldsymbol{\xi}}{\partial \boldsymbol{x}}$ is the Jacobian matrix of the mapping between the parametric element and its corresponding physical counterpart, and C_I is a positive constant.

At last, we assume that the pressure fine-scale parameter retains its usual definition,[9] namely,

$$\tau_c = \frac{1}{\tau_m \mathrm{tr}\boldsymbol{G}}, \tag{3.19}$$

where tr is the trace operation.

Remark. The above formulation features a modified RBVMS, in which the construction of velocity fine scales accounts for the coupling of the Navier–Stokes and density equations through the Boussinesq term. This coupling leads to the non-diagonal term in the stabilization matrix in Eq. (3.15). The formulation is motivated by the stabilized methods for convection–diffusion systems in,[46, 47, 84] which was recently applied to LES simulations of stratified flows in,[32, 115, 120] showing enhanced performance in capturing the turbulence statistics in this class of problems.

Remark. The RBVMS formulation of this work is deployed to a stationary mesh for particle-laden flows. One should note that the formulation and its more advanced versions, such as Space–Time (ST–VMS) technique[54, 90, 93–95] and Arbitrary Lagrangian–Eulerian technique (ALE-VMS),[10, 17, 21–24, 30, 87] have successfully been used in LES simulations of a wide range of challenging fluid dynamics and fluid–structure interaction problems. These methods particularly show significant advantages when deployed to flow problems with moving interfaces and boundaries. Several recent application domains include environmental flows,[33, 79, 120, 124] wind energy[4, 15, 18, 22, 25, 36, 57–59, 66, 67, 73, 86, 89, 91, 92, 99, 100, 118, 119], tidal energy,[4, 5, 80, 117, 118, 123] cavitation flows[5, 6], hypersonic flows,[35] biomechanics,[43, 52, 64, 88, 107, 108] gas turbine,[76, 77, 116] and transportation engineering.[60, 61, 63, 96–98]

Remark. Although this paper utilizes C_1-continuous quadratic NURBS, it can easily accommodate other representations such as T-splines or subdivision surfaces.[8, 34, 44]

3.3. *Other numerical details*

We digitize the RBVMS in Eq. (3.7) with quadratic NURBS basis functions with uniform control points. The velocity, pressure, and density unknowns are solved in a fully-coupled fashion. The Generalized-α method is used for the time integration scheme. Newton's method is utilized to linearize the nonlinear nodal equations. The resulting linear system is solved by a generalized minimal residual method (GMRES) with block preconditioning.[82, 83]

4. Computational Setup

We deploy the RBVMS with the NURBS discretization to simulate particle-laden flows in the lock-exchange configuration over a flat bottom surface. For simplicity, we call the method VMS–IGA in the rest of the paper. The computational setup is described as follows.

As shown in Fig. 1, the computational domain is a rectangular box with dimensions of $L_x \times L_y \times L_z = 14 \times 2 \times 2$, where uniformly suspended particle sediments are initially enclosed in a small portion ($L_x^s \times L_y^s \times L_z^s = 1 \times 2 \times 2$) of the domain and separated by a barrier with the clear fluid on the other side. Due to gravity, an invasion of the "heavy" fluid to the "light" fluid will happen, leading to particle-laden turbulence. In all the simulations, settling velocity u_s, Reynolds number Re, and Schmidt number $\mathrm{S_c}$ are set to 0.02, 10,000, and 1, respectively. The problem is spatially discretized by C_1 continuous quadratic B-splines with elements of $350 \times 50 \times 50$. Fig. 2 shows a snapshot of the mesh used. Here, the control points are placed to achieve uniform spatial resolution for a fair comparison with reference results. For the discussion of control point distribution and parameterization, readers are referred to the work.[74, 75, 111] The time step size is $\Delta t = 2.0 \times 10^{-3}$.

The boundary conditions are specified as follows. For stream-wise and span-wise directions, no penetration and free-slip boundary conditions are used for the velocity field. For the top wall, a no-slip boundary is used for the velocity field. For the bottom wall, a no-slip boundary is used for the velocity field. A no-flux

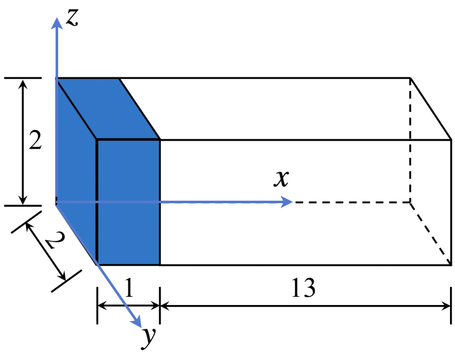

Fig. 1. (Color online) Computational setup. The blue color represents the initial distribution of suspended particle sediments.

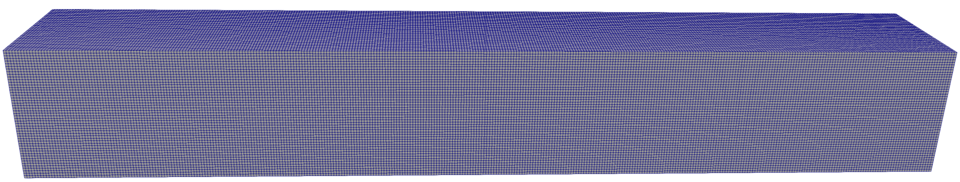

Fig. 2. The mesh employed in the simulation.

boundary condition is used for the density field at the side and top walls. No erosion and re-suspension are allowed for the density field on bottom wall, namely, $u_s \nabla\rho \cdot \boldsymbol{e}_g + \frac{\partial\rho}{\partial t} = 0$.

This case represents one of the most famous canonical configurations of particle-laden flows for conducting laboratory experiments and high-resolution simulations. In this paper, the results of this case from the DNS in[38] with a resolution of $2305 \times 513 \times 385$ and the high fidelity simulation in[72] with a resolution of $1440 \times 200 \times 221$ are used for assessing the accuracy of VMS–IGA.

5. Results and Discussions

We present the simulation results in this section. The discussion focus will be placed on evaluating the accuracy of VMS–IGA by comparing it with existing high-resolution simulation results.

5.1. *Flow visualization*

We start the discussion with instantaneous flow visualizations. Fig. 3 shows the isosurface of $\rho = 0.25$ colored by velocity magnitude. The DNS results from[38] is also plotted for comparison. For this case, the VMS–IGA, with a relatively coarse mesh, produces quite similar interface patterns as the DNS does. The typical 3D lobe-and-cleft structures are captured well by the VMS–IGA, as shown in Fig. 4. Fig. 5 plots the vorticity using the isosurface of Q-criterion ($Q = 1$) at $t = 20$.

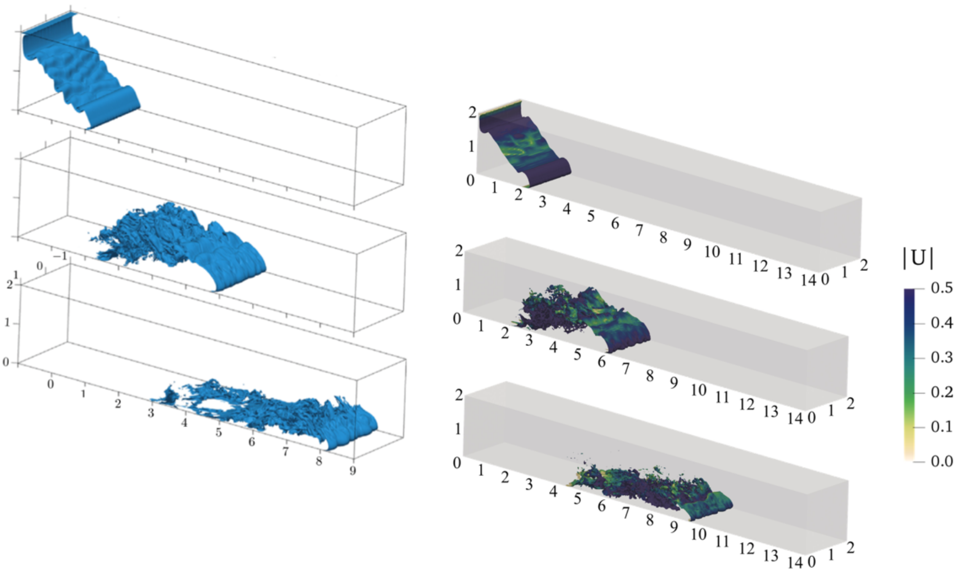

Fig. 3. Isosurface of $\rho = 0.25$ at $t = 2, 8$, and 14 colored by velocity magnitude. Left: DNS. Right: VMS–IGA. One should note that the color in the DNS results[38] is not based on velocity magnitude.

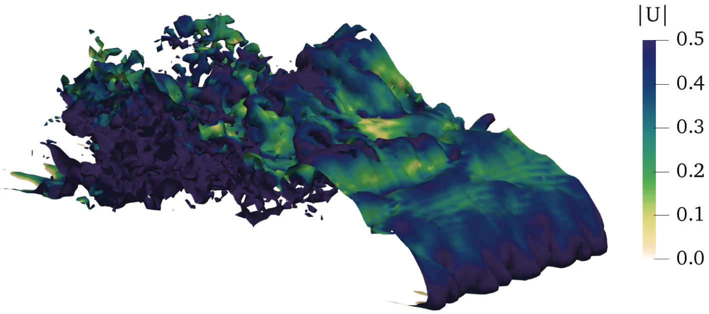

Fig. 4. 3D lobe-and-cleft structures at $t = 8$.

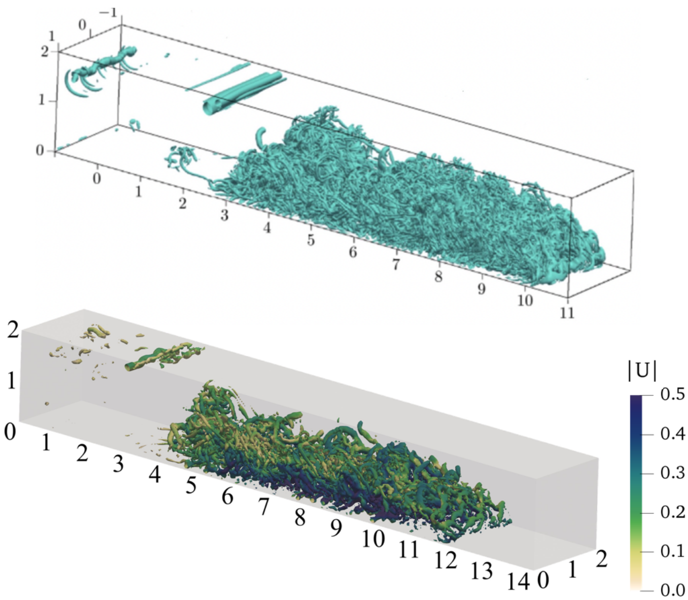

Fig. 5. Vortex structure based on isosurface using Q-criterion ($Q = 1$) at $t = 20$ colored by velocity magnitude. Top: DNS. Bottom: VMS–IGA. (One should note that the color in the DNS results[38] is not based on velocity magnitude).

These vortex structures illustrate the complexity of the turbulence in this type of particle-laden flow. Again, similar vortex structures are found between the DNS and VMS–IGA results.

5.2. *Turbulence statistics*

We further report quantified turbulence statistics of the velocity and density fields. Fig. 6 shows the time history of the current front location. A good agreement is found between DNS and VMS–IGA results, which show that the front has almost a constant front speed before $t = 10$ and slightly decreases after that.

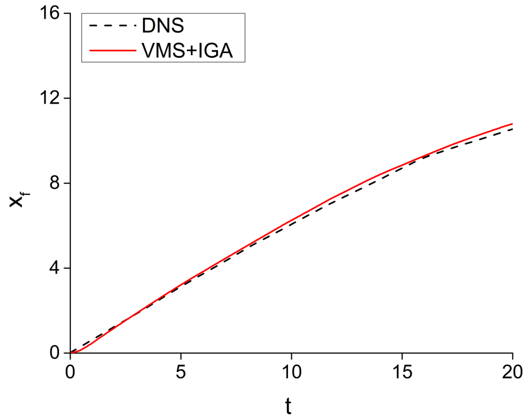

Fig. 6. Time history of the front location predicted by VMS–IGA and the DNS from.[38]

Suspension and sedimentation are two important quantities of interest in particle-laden currents. The total suspended particle mass can be computed as

$$m_p(t) = \int_\Omega \rho \, d\Omega. \tag{5.1}$$

The time history of the suspended mass $m_p(t)$ normalized by the initial mass $m_p(0)$, predicted by DNS and VMS–IGA, is plotted in Fig. 7. Fig. 8 shows the sedimentation rate in a log–log fashion. The sedimentation rate is quantified by the time derivative of the total mass of sedimented particles per unit span as

$$\dot{m_s}(t) = \frac{1}{L_y} \int_0^{L_y} \int_0^{L_x} \rho_w(x, y, t) u_s \, dx dy, \tag{5.2}$$

where $\rho_w(x, y, t)$ is the density at the bottom surface.

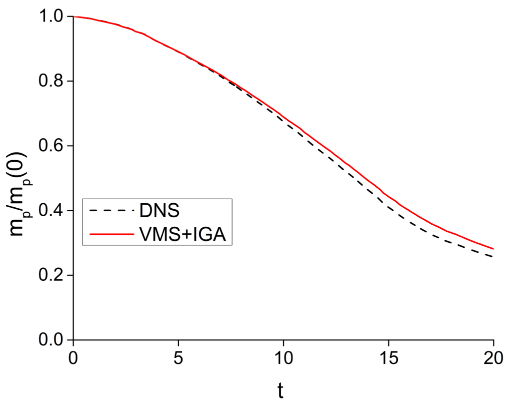

Fig. 7. Time history of dimensionless suspended particle mass predicted by VMS–IGA and the DNS from.[38]

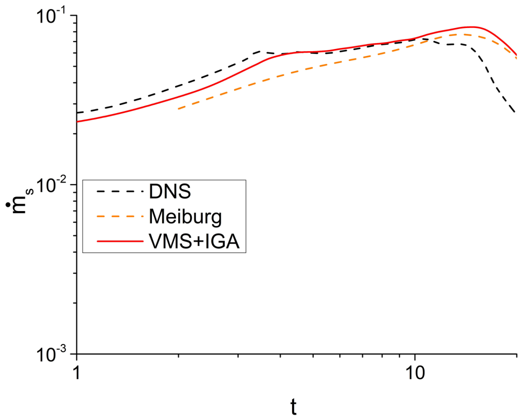

Fig. 8. Sedimentation rate predicted by VMS–IGA and the DNS from.[38]

The VMS–IGA shows good agreement with DNS for the suspended mass. The VMS–IGA also achieves reasonable agreement with the DNS result for the sedimentation rate before $t = 9$, but a noticeable discrepancy is observed after that, as seen Fig. 8. To further evaluate the IGA's accuracy, we also plot the high-fidelity results using a resolution of $1440 \times 200 \times 221$ from,[72] which shows a similar prediction as the VMS–IGA does.

The sedimentation process can be characterized by the stream-wise deposit of the sediment particles, which is quantified as

$$D_t(x,t) = \frac{1}{L_x^s L_y^s} \int_0^t \langle \rho_w(x,\tau) \rangle_y u_s \, d\tau, \tag{5.3}$$

where $\langle \rho_w(x,\tau) \rangle_y$ is averaged density over y-direction at the bottom surface. Fig. 9 depicts the particle deposit along stream-wise (x) direction at $t = 7.3$ and $t = 11.0$. The deposit profiles display a complicated pattern along the stream-wise, making

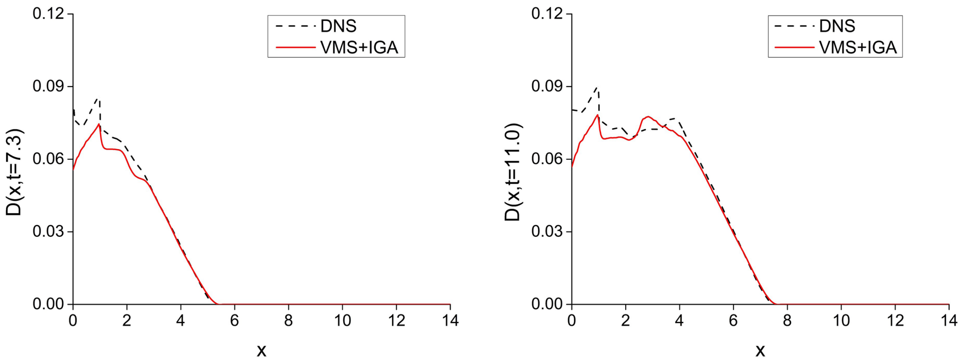

Fig. 9. Deposit profile for $t = 7.3$ and $t = 11$ predicted by VMS–IGA and the DNS results from.[38]

it hard to obtain a monotonic tendency. Overall, the VMS–IGA predicts quite a similar deposit profile as the DNS does.

The fluid motion of particle-laden flows is essentially an energy transfer process. The initial potential energy is gradually converted to kinetic energy. If no potential energy is fed into the domain, the fluid motion will ultimately decay due to energy dissipation, caused by both convection gradients and the energy loss experienced by the particles due to progressive settling. At time t, the potential energy $E_p(t)$, kinetic energy $k(t)$, turbulent dissipation $E_\nu(t)$, and dissipation from suspended particles $E_s(t)$ can be computed as

$$E_p(t) = \int_\Omega \rho z \, d\Omega, \tag{5.4}$$

$$k(t) = \int_\Omega \frac{1}{2}\boldsymbol{u} \cdot \boldsymbol{u} \, d\Omega, \tag{5.5}$$

$$E_\nu(t) = \int_0^t \int_\Omega \frac{2}{\mathrm{Re}} \boldsymbol{S} : \boldsymbol{S} \, d\Omega \, d\tau, \tag{5.6}$$

$$E_s(t) = \int_0^t \int_\Omega u_s \rho \, d\Omega \, d\tau, \tag{5.7}$$

where $\boldsymbol{S} = \frac{1}{2}[\nabla \boldsymbol{u} + (\nabla \boldsymbol{u})^T]$ is the symmetric part of the velocity gradient. Here, the potential energy is evaluated by the elevation of the center of mass of the heavy fluid relative to the light fluid.

The time history of $E_p(t)$, $k(t)$, $E_\nu(t)$, and $E_s(t)$, normalized by the initial potential energy $E_p(0)$, is plotted from Figs. 10–13. Although a noticeable discrepancy is found in $E_s(t)$ between VMS–IGA and DNS, VMS–IGA produces accurate predictions of other energy distribution, showing good agreement with the DNS results despite a relatively coarse mesh being used.

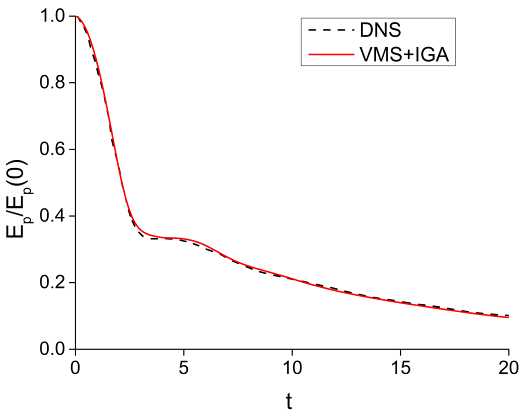

Fig. 10. Time history of normalized potential energy $E_p(t)/E_p(0)$ predicted by VMS–IGA and the DNS from.[38]

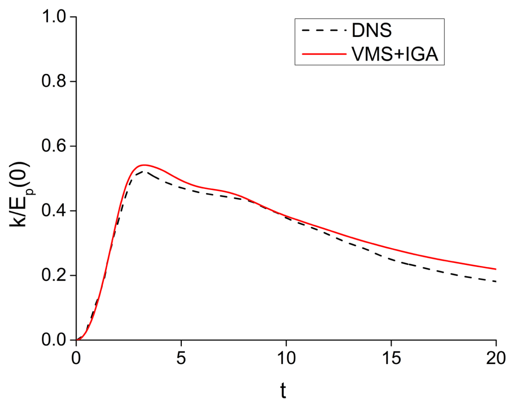

Fig. 11. Time history of normalized kinetic energy $k(t)/E_p(0)$ predicted by VMS–IGA and the DNS from.[38]

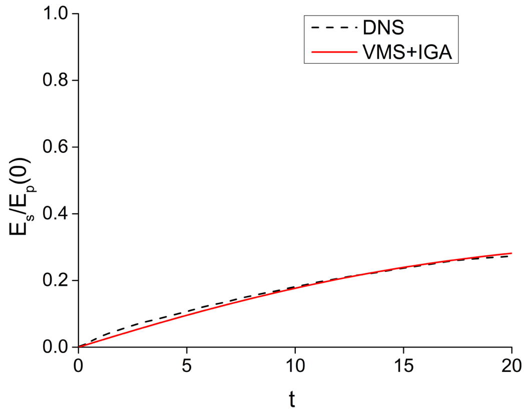

Fig. 12. Time history of normalized dissipated energy $E_s(t)/E_p(0)$ predicted by VMS–IGA and the DNS from.[38]

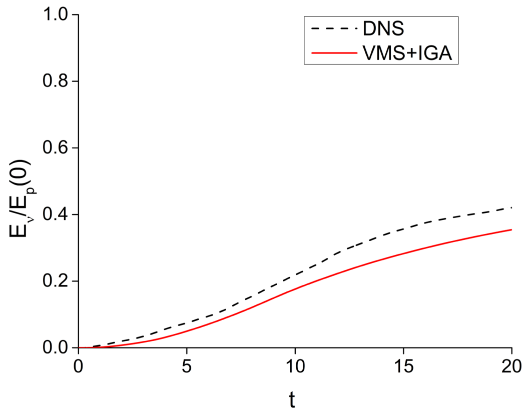

Fig. 13. Time history of normalized dissipated energy $E_\nu(t)/E_p(0)$ predicted by VMS–IGA and the DNS from.[38]

6. Conclusions

This paper integrated IGA with a modified RBVMS formulation to simulate turbulent particle-laden flows over a flat bottom surface. We compared the simulation results with available DNS and high-resolution simulation results from the literature. It was found that the higher-order basis functions of IGA, combined with VMS as the LES model, offer higher accuracy in capturing critical quantities of interest in particle-laden flows with fewer degrees of freedom than existing models. The results presented in this paper provide a strong testimony of the advantage of using IGA in multi-phase flow simulations.

Acknowledgments

J. Yan is partially supported by U.S. Department of Energy under the grant of DE-FOA-0002234. The support is greatly acknowledged.

References

1. M. Alaydin, M. Behzadinasab and Y. Bazilevs, Isogeometric analysis of multilayer composite shell structures: Plasticity, damage, delamination and impact modeling, *Internat. J. Solids Structures* **252** (2022) 111782.
2. L. Aydinbakar, K. Takizawa, T. E. Tezduyar and T. Kuraishi, Space–time VMS isogeometric analysis of the Taylor–Couette flow, *Comput. Mech.* **67** (2021) 1515–1541.
3. L. Aydinbakar, K. Takizawa, T. E. Tezduyar and D. Matsuda, U-duct turbulent-flow computation with the ST-VMS method and isogeometric discretization, *Comput. Mech.* **67** (2021) 823–843.
4. A. B. Mohamed, C. Bear, M. Bear and A. Korobenko, Performance analysis of two vertical-axis hydrokinetic turbines using variational multiscale method, *Comput. Fluids* **200** (2020) 104432.
5. A. Bayram and A. Korobenko, Variational multiscale framework for cavitating flows, *Comput. Mech.* **66** (2020) 49–67.
6. A. Bayram and A. Korobenko, A numerical formulation for cavitating flows around marine propellers based on variational multiscale method, *Comput. Mech.* **68** (2021) 405–432.
7. Y. Bazilevs and I. Akkerman, Large eddy simulation of turbulent Taylor–Couette flow using isogeometric analysis and the residual-based variational multiscale method, *J. Comput. Phys.* **229** (2010) 3402–3414.
8. Y. Bazilevs, V. M. Calo, A. Cottrell, J. Evans, T. Hughes, S. Lipton, M. Scott and T. Sederberg, Isogeometric analysis using T-splines, *Comput. Methods Appl. Mech. Engrg.* **199** (2010) 229–263.
9. Y. Bazilevs, V. M. Calo, J. A. Cottrell, T. J. R. Hughes, A. Reali and G. Scovazzi, Variational multiscale residual-based turbulence modeling for large eddy simulation of incompressible flows, *Comput. Methods Appl. Mech. Engrg.* **197** (2007) 173–201.
10. Y. Bazilevs, V. M. Calo, T. J. R. Hughes and Y. Zhang, Isogeometric fluid–structure interaction: Theory, algorithms, and computations, *Comput. Mech.* **43** (2008) 3–37.
11. Y. Bazilevs, V. M. Calo, Y. Zhang and T. J. R. Hughes, Isogeometric fluid–structure interaction analysis with applications to arterial blood flow, *Comput. Mech.* **38** (2006) 310–322.

12. Y. Bazilevs, X. Deng, A. Korobenko, F. Lanza di Scalea, M. D. Todd and S. G. Taylor, Isogeometric fatigue damage prediction in large-scale composite structures driven by dynamic sensor data, *J. Appl. Mech.* **82** (2015) 091008.
13. Y. Bazilevs, J. R. Gohean, T. J. R. Hughes, R. D. Moser and Y. Zhang, Patient-specific isogeometric fluid–structure interaction analysis of thoracic aortic blood flow due to implantation of the Jarvik 2000 left ventricular assist device, *Comput. Methods Appl. Mech. Engrg.* **198** (2009) 3534–3550.
14. Y. Bazilevs and T. J. R. Hughes, NURBS-based isogeometric analysis for the computation of flows about rotating components, *Comput. Mech.* **43** (2008) 143–150.
15. Y. Bazilevs, M.-C. Hsu, I. Akkerman, S. Wright, K. Takizawa, B. Henicke, T. Spielman and T. E. Tezduyar, 3D simulation of wind turbine rotors at full scale. Part I: Geometry modeling and aerodynamics, *Internat. J. Numer. Methods Fluids* **65** (2011) 207–235.
16. Y. Bazilevs, M.-C. Hsu and M. A. Scott, Isogeometric fluid–structure interaction analysis with emphasis on non-matching discretizations, and with application to wind turbines, *Comput. Methods Appl. Mech. Engrg.* **249–252** (2012) 28–41.
17. Y. Bazilevs, M.-C. Hsu, K. Takizawa and T. E. Tezduyar, ALE-VMS and ST-VMS methods for computer modeling of wind-turbine rotor aerodynamics and fluid–structure interaction, *Math. Models Methods Appl. Sci.* **22** (2012) 1230002.
18. Y. Bazilevs, A. Korobenko, X. Deng, J. Yan, M. Kinzel and J. O. Dabiri, FSI modeling of vertical-axis multi-scales, *J. Appl. Mech.* **81** (2014) 081006.
19. Y. Bazilevs, C. Michler, V. M. Calo and T. J. R. Hughes, Isogeometric variational multiscale modeling of wall-bounded turbulent flows with weakly enforced boundary conditions on unstretched meshes, *Comput. Methods Appl. Mech. Engrg.* **199** (2010) 780–790.
20. Y. Bazilevs, G. Moutsanidis, J. Bueno, K. Kamran, D. Kamensky, M. Hillman, H. Gomez and J. Chen, A new formulation for air-blast fluid–structure interaction using an immersed approach: Part II — Coupling of IGA and meshfree discretizations, *Comput. Mech.* **60** (2017) 101–116.
21. Y. Bazilevs, K. Takizawa and T. E. Tezduyar, Challenges and directions in computational fluid–structure interaction, *Math. Models Methods Appl. Sci.* **23** (2013) 215–221.
22. Y. Bazilevs, K. Takizawa and T. E. Tezduyar, *Computational Fluid–Structure Interaction: Methods and Applications* (Wiley, 2013).
23. Y. Bazilevs, K. Takizawa and T. E. Tezduyar, New directions and challenging computations in fluid dynamics modeling with stabilized and multiscale methods, *Math. Models Methods Appl. Sci.* **25** (2015) 2217–2226.
24. Y. Bazilevs, K. Takizawa and T. E. Tezduyar, Computational analysis methods for complex unsteady flow problems, *Math. Models Methods Appl. Sci.* **29** (2019) 825–838.
25. Y. Bazilevs, K. Takizawa, T. E. Tezduyar, M.-C. Hsu, N. Kostov and S. McIntyre, Aerodynamic and FSI analysis of wind turbines with the ALE-VMS and ST-VMS methods, *Arch. Comput. Methods Eng.* **21** (2014) 359–398.
26. Y. Bazilevs, K. Takizawa, T. E. Tezduyar, M. Hsu, Y. Otoguro, H. Mochizuki and M. C. H. Wu, ALE and Space–Time variational multiscale isogeometric analysis of wind turbines and turbomachinery, in *Parallel Algorithms in Computational Science and Engineering*, Modeling and Simulation in Science, Engineering and Technology, eds. A. Grama and A. Sameh (Springer, 2020), pp. 195–233.
27. Y. Bazilevs, K. Takizawa, M. C. H. Wu, T. Kuraishi, R. Avsar, Z. Xu and T. E. Tezduyar, Gas turbine computational flow and structure analysis with isogeometric

discretization and a complex-geometry mesh generation method, *Comput. Mech.* **67** (2021) 57–84.
28. M. Behzadinasab, G. Moutsanidis, N. Trask, J. Foster and Y. Bazilevs, Coupling of IGA and peridynamics for air-blast fluid–structure interaction using an immersed approach, *Forces Mech.* **4** (2021) 100045.
29. A. N. Brooks and T. J. R. Hughes, Streamline upwind/Petrov–Galerkin formulations for convection dominated flows with particular emphasis on the incompressible Navier–Stokes equations, *Comput. Methods Appl. Mech. Engrg.* **32** (1982) 199–259.
30. R. Calderer, L. Zhu, R. Gibson and A. Masud, Residual-based turbulence models and arbitrary Lagrangian–Eulerian framework for free surface flows, *Math. Models Methods Appl. Sci.* **25** (2015) 2287317.
31. J. Capecelatro and O. Desjardins, An Euler–Lagrange strategy for simulating particle-laden flows, *J. Comput. Phys.* **238** (2013) 1–31.
32. H. Cen, Q. Zhou and A. Korobenko, Simulation of stably stratified turbulent channel flow using residual-based variational multiscale method and isogeometric analysis, *Comput. Fluids* **214** (2021) 104765.
33. H. Cen, Q. Zhou and A. Korobenko, Wall-function-based weak imposition of dirichlet boundary condition for stratified turbulent flows, *Comput. Fluids* **234** (2022) 105257.
34. F. Cirak, M. Ortiz and P. Schröder, Subdivision surfaces: A new paradigm for thin-shell finite-element analysis, *Internat. J. Numer. Methods Engrg.* **47** (2000) 2039–2072.
35. D. Codoni, G. Moutsanidis, M.-C. Hsu, Y. Bazilevs, C. Johansen and A. Korobenko, Stabilized methods for high-speed compressible flows: Toward hypersonic simulations, *Comput. Mech.* **67** (2021) 785–809.
36. M. Dhalwala, A. Bayram, P. Oshkai and A. Korobenko, Performance and near-wake analysis of a vertical-axis hydrokinetic turbine under a turbulent inflow, *Ocean Eng.* **257** (2022) 111703.
37. S. Elghobashi, On predicting particle-laden turbulent flows, *Appl. Sci. Res.* **52** (1994) 309–329.
38. L. Espath, L. Pinto, S. Laizet and J. H. Silvestrini, Two-and three-dimensional direct numerical simulation of particle-laden gravity currents, *Comput. Geosci.* **63** (2014) 9–16.
39. F. Evrard, F. Denner and B. Van, Euler–Lagrange modelling of dilute particle-laden flows with arbitrary particle-size to mesh-spacing ratio, *J. Comput. Phys.: X* **8** (2020) 100078.
40. A. J. Herrema, E. L. Johnson, D. Proserpio, M. C. H. Wu, J. Kiendl and M.-C. Hsu, Penalty coupling of non-matching isogeometric Kirchhoff–Love shell patches with application to composite wind turbine blades, *Comput. Methods Appl. Mech. Engrg.* **346** (2019) 810–840.
41. A. J. Herrema, J. Kiendl and M.-C. Hsu, A framework for isogeometric-analysis-based optimization of wind turbine blade structures, *Wind Energy* **22** (2019) 153–170.
42. M.-C. Hsu, I. Akkerman and Y. Bazilevs, High-performance computing of wind turbine aerodynamics using isogeometric analysis, *Comput. Fluids* **49** (2011) 93–100.
43. M.-C. Hsu, D. Kamensky, Y. Bazilevs, M. S. Sacks and T. J. R. Hughes, Fluid–structure interaction analysis of bioprosthetic heart valves: Significance of arterial wall deformation, *Comput. Mech.* **54** (2014) 1055–1071.
44. M.-C. Hsu, D. Kamensky, F. Xu, J. Kiendl, C. Wang, M. C. H. Wu, J. Mineroff, A. Reali, Y. Bazilevs and M. S. Sacks, Dynamic and fluid–structure interaction

simulations of bioprosthetic heart valves using parametric design with T-splines and Fung-type material models, *Comput. Mech.* **55** (2015) 1211–1225.

45. T. J. R. Hughes, J. A. Cottrell and Y. Bazilevs, Isogeometric analysis: CAD, finite elements, NURBS, exact geometry, and mesh refinement, *Comput. Methods Appl. Mech. Engrg.* **194** (2005) 4135–4195.
46. T. J. R. Hughes and M. Mallet, A new finite element formulation for computational fluid dynamics: III. The generalized streamline operator for multidimensional advective-diffusive systems, *Comput. Methods Appl. Mech. Engrg.* **58** (1986) 305–328.
47. T. J. R. Hughes, G. Scovazzi and T. E. Tezduyar, Stabilized methods for compressible flows, *J. Sci. Comput.* **43** (2010) 343–368, doi:10.1007/s10915-008-9233-5.
48. A. Johnson and T. E. Tezduyar, Simulation of multiple spheres falling in a liquid-filled tube, *Comput. Methods Appl. Mech. Engrg.* **134** (1996) 351–373.
49. A. Johnson and T. E. Tezduyar, 3D simulation of fluid–particle interactions with the number of particles reaching 100, *Comput. Methods Appl. Mech. Engrg.* **145** (1997) 301–321.
50. A. Johnson and T. E. Tezduyar, Advanced mesh generation and update methods for 3D flow simulations, *Comput. Mech.* **23** (1999) 130–143.
51. A. Johnson and T. E. Tezduyar, Methods for 3D computation of fluid–object interactions in spatially periodic flows, *Comput. Methods Appl. Mech. Engrg.* **190** (2001) 3201–3221.
52. E. L. Johnson, M. C. H. Wu, F. Xu, N. M. Wiese, M. R. Rajanna, A. J. Herrema, B. Ganapathysubramanian, T. J. R. Hughes, M. S. Sacks and M.-C. Hsu, Thinner biological tissues induce leaflet flutter in aortic heart valve replacements, *Proc. Natl. Acad. Sci.* **117** (2020) 19007–19016.
53. V. Kalro, S. Aliabadi, W. Garrard, T. Tezduyar, S. Mittal and K. Stein, Parallel finite element simulation of large ram-air parachutes, *Internat. J. Numer. Methods Fluids* **24** (1997) 1353–1369.
54. V. Kalro and T. E. Tezduyar, A parallel 3D computational method for fluid–structure interactions in parachute systems, *Comput. Methods Appl. Mech. Engrg.* **190** (2000) 321–332.
55. A. Kartushinsky, S. Tisler, J. Oliveira and C. Van, Eulerian–Eulerian modelling of particle-laden two-phase flow, *Powder Technol.* **301** (2016) 999–1007.
56. J. Kiendl, Y. Bazilevs, M.-C. Hsu, R. Wüchner and K.-U. Bletzinger, The bending strip method for isogeometric analysis of Kirchhoff–Love shell structures comprised of multiple patches, *Comput. Methods Appl. Mech. Engrg.* **199** (2010) 2403–2416.
57. A. Korobenko, Y. Bazilevs, K. Takizawa and T. E. Tezduyar, Recent advances in ALE-VMS and ST-VMS computational aerodynamic and FSI analysis of wind turbines, in *Frontiers in Computational Fluid–Structure Interaction and Flow Simulation: Research from Lead Investigators under Forty — 2018*, ed. T. E. Tezduyar, Modeling and Simulation in Science, Engineering and Technology (Springer, 2018), pp. 253–336.
58. A. Korobenko, Y. Bazilevs, K. Takizawa and T. E. Tezduyar, Computer modeling of wind turbines: 1. ALE-VMS and ST-VMS aerodynamic and FSI analysis, *Arch. Comput. Methods Engrg.* **26** (2019) 1059–1099.
59. A. Korobenko, M.-C. Hsu, I. Akkerman and Y. Bazilevs, Aerodynamic simulation of vertical-axis wind turbines, *J. Appl. Mech.* **81** (2013) 021011.
60. T. Kuraishi, K. Takizawa and T. E. Tezduyar, Space–time computational analysis of tire aerodynamics with actual geometry, road contact and tire deformation, in *Frontiers in Computational Fluid–Structure Interaction and Flow Simulation: Research*

from Lead Investigators under Forty — 2018, ed. T. E. Tezduyar, Modeling and Simulation in Science, Engineering and Technology (Springer, 2018), pp. 337–376.
61. T. Kuraishi, K. Takizawa and T. E. Tezduyar, Space–time computational analysis of tire aerodynamics with actual geometry, road contact, tire deformation, road roughness and fluid film, *Comput. Mech.* **64** (2019) 1699–1718.
62. T. Kuraishi, K. Takizawa and T. E. Tezduyar, Space–time isogeometric flow analysis with built-in Reynolds-equation limit, *Math. Models Methods Appl. Sci.* **29** (2019) 871–904.
63. T. Kuraishi, K. Takizawa and T. E. Tezduyar, Tire aerodynamics with actual tire geometry, road contact and tire deformation, *Comput. Mech.* **63** (2019) 1165–1185.
64. T. Kuraishi, T. Terahara, K. Takizawa and T. E. Tezduyar, Computational flow analysis with boundary layer and contact representation: I. Tire aerodynamics with road contact, *J. Mech.* **38** (2022) 77–87.
65. T. Kuraishi, S. Yamasaki, K. Takizawa, T. E. Tezduyar, Z. Xu and R. Kaneko, Space–time isogeometric analysis of car and tire aerodynamics with road contact and tire deformation and rotation, *Comput. Mech.* **70** (2022) 49–72.
66. T. Kuraishi, F. Zhang, K. Takizawa and T. E. Tezduyar, Wind turbine wake computation with the ST-VMS method, isogeometric discretization and multidomain method: I. Computational framework, *Comput. Mech.* **68** (2021) 113–130.
67. T. Kuraishi, F. Zhang, K. Takizawa and T. E. Tezduyar, Wind turbine wake computation with the ST-VMS method, isogeometric discretization and multidomain method: II. Spatial and temporal resolution, *Comput. Mech.* **68** (2021) 175–184.
68. A. Lattanzi, V. Tavanashad, S. Subramaniam and J. Capecelatro, Stochastic model for the hydrodynamic force in Euler–Lagrange simulations of particle-laden flows, *Phys. Rev. Fluids* **7** (2022) 014301.
69. E. Masi, B. Bedát, M. Moreau and O. Simonin, Euler–Euler large-eddy simulation approach for non isothermal particle-laden turbulent jet, in *Fluids Engineering Division Summer Meeting collocated with the Heat Transfer, Energy Sustainability, and 3rd Energy Nanotechnology Conferences*, Vol. 1, Symposia, Parts A and B. Jacksonville, Florida, USA. August 10–14 (2008) pp. 111–120.
70. G. Moutsanidis, D. Kamensky, J. Chen and Y. Bazilevs, Hyperbolic phase field modeling of brittle fracture: Part II — Immersed IGA–RKPM coupling for air-blast–structure interaction, *J. Mech. Phys. Solids* **121** (2018) 114–132.
71. G. Moutsanidis, C. Long and Y. Bazilevs, IGA-MPM: The isogeometric material point method, *Comput. Methods Appl. Mech. Engrg.* **372** (2020) 113346.
72. F. Necker, C. Härtel, L. Kleiser and E. Meiburg, High-resolution simulations of particle-driven gravity currents, *Int. J. Multiph. Flow* **28** (2002) 279–300.
73. Y. Otoguro, H. Mochizuki, K. Takizawa and T. E. Tezduyar, Space–time variational multiscale isogeometric analysis of a tsunami-shelter vertical-axis wind turbine, *Comput. Mech.* **66** (2020) 1443–1460.
74. Y. Otoguro, K. Takizawa and T. E. Tezduyar, Space–time VMS computational flow analysis with isogeometric discretization and a general-purpose NURBS mesh generation method, *Comput. Fluids* **158** (2017) 189–200.
75. Y. Otoguro, K. Takizawa and T. E. Tezduyar, Element length calculation in B-spline meshes for complex geometries, *Comput. Mech.* **65** (2020) 1085–1103.
76. Y. Otoguro, K. Takizawa, T. E. Tezduyar, K. Nagaoka, R. Avsar and Y. Zhang, Space–time VMS flow analysis of a turbocharger turbine with isogeometric discretization: Computations with time-dependent and steady-inflow representations of the intake/exhaust cycle, *Comput. Mech.* **64** (2019) 1403–1419.

77. Y. Otoguro, K. Takizawa, T. E. Tezduyar, K. Nagaoka and S. Mei, Turbocharger turbine and exhaust manifold flow computation with the Space–Time Variational Multiscale Method and Isogeometric Analysis, *Comput. Fluids* **179** (2019) 764–776.
78. S. B. Raknes, X. Deng, Y. Bazilevs, D. J. Benson, K. M. Mathisen and T. Kvamsdal, Isogeometric rotation-free bending-stabilized cables: Statics, dynamics, bending strips and coupling with shells, *Comput. Methods Appl. Mech. Engrg.* **263** (2013) 127–143.
79. M. Ravensbergen, T. A. Helgedagsrud, Y. Bazilevs and A. Korobenko, A variational multiscale framework for atmospheric turbulent flows over complex environmental terrains, *Comput. Methods Appl. Mech. Engrg.* **368** (2020) 113182.
80. M. Ravensbergen, A. Mohamed and A. Korobenko, The actuator line method for wind turbine modelling applied in a variational multiscale framework, *Comput. Fluids* **201** (2020) 104465.
81. E. Riber, M. Moreau, O. Simonin and B. Cuenot, Towards large eddy simulation of non-homogeneous particle laden turbulent gas flows using Euler–Euler approach, in *11th Workshop on Two-Phase Flow Predictions*, Vol. 51, 2005, Merseburg, Germany, pp. 183–200.
82. Y. Saad, Krylov subspace methods for solving large unsymmetric linear systems, *Math. Comput.* **37** (1981) 105–126.
83. Y. Saad and M. Schultz, GMRES: A generalized minimal residual algorithm for solving nonsymmetric linear systems, *SIAM J. Sci. Statist. Comput.* **7** (1986) 856–869.
84. F. Shakib, T. J. R. Hughes and Z. Johan, A multi-element group preconditionined GMRES algorithm for nonsymmetric systems arising in finite element analysis, *Comput. Methods Appl. Mech. Engrg.* **75** (1989) 415–456.
85. J. Sweet, D. Richter and D. Thain, GPU acceleration of Eulerian–Lagrangian particle-laden turbulent flow simulations, *Int. J. Multiph. Flow* **99** (2018) 437–445.
86. K. Takizawa, Computational engineering analysis with the new-generation space–time methods, *Comput. Mech.* **54** (2014) 193–211.
87. K. Takizawa, Y. Bazilevs and T. E. Tezduyar, Space–time and ALE-VMS techniques for patient-specific cardiovascular fluid–structure interaction modeling, *Arch. Comput. Methods Engrg.* **19** (2012) 171–225.
88. K. Takizawa, Y. Bazilevs, T. E. Tezduyar and M.-C. Hsu, Computational cardiovascular flow analysis with the variational multiscale methods, *J. Adv. Eng. Comput.* **3** (2019) 366–405.
89. K. Takizawa, Y. Bazilevs, T. E. Tezduyar, M.-C. Hsu, O. Øiseth, K. M. Mathisen, N. Kostov and S. McIntyre, Engineering analysis and design with ALE-VMS and space–time methods, *Arch. Comput. Methods Eng.* **21** (2014) 481–508.
90. K. Takizawa, M. Fritze, D. Montes, T. Spielman and T. E. Tezduyar, Fluid–structure interaction modeling of ringsail parachutes with disreefing and modified geometric porosity, *Comput. Mech.* **50** (2012) 835–854.
91. K. Takizawa, B. Henicke, D. Montes, T. E. Tezduyar, M.-C. Hsu, and Y. Bazilevs, Numerical-performance studies for the stabilized space–time computation of wind-turbine rotor aerodynamics, *Comput. Mech.* **48** (2011) 647–657.
92. K. Takizawa, B. Henicke, T. E. Tezduyar, M.-C. Hsu and Y. Bazilevs, Stabilized space–time computation of wind-turbine rotor aerodynamics, *Comput. Mech.* **48** (2011) 333–344.
93. K. Takizawa and T. E. Tezduyar, Computational methods for parachute fluid–structure interactions, *Arch. Comput. Methods Engrg.* **19** (2012) 125–169.

94. K. Takizawa, T. E. Tezduyar, J. Boben, N. Kostov, C. Boswell and A. Buscher, Fluid–structure interaction modeling of clusters of spacecraft parachutes with modified geometric porosity, *Comput. Mech.* **52** (2013) 1351–1364.
95. K. Takizawa, T. E. Tezduyar, C. Boswell, Y. Tsutsui and K. Montel, Special methods for aerodynamic-moment calculations from parachute FSI modeling, *Comput. Mech.* **55** (2015) 1059–1069.
96. T. Kuraishi, K. Takizawa, S. Tabata, S. Asada and T. E. Tezduyar, Multiscale thermo-fluid analysis of a tire, in *Proc. 19th Japan Society of Computational Engineering and Science Conf.*, 2014, Hiroshima, Japan.
97. K. Takizawa, T. E. Tezduyar and T. Kuraishi, Multiscale ST methods for thermo-fluid analysis of a ground vehicle and its tires, *Math. Models Methods Appl. Sci.* **25** (2015) 2227–2255.
98. K. Takizawa, T. E. Tezduyar and T. Kuraishi, Computational flow analysis with boundary layer and contact representation: I. Tire aerodynamics with road contact, *Journal of Mechanics* **38** (2022) 77–87.
99. K. Takizawa, T. E. Tezduyar, S. McIntyre, N. Kostov, R. Kolesar and C. Habluetzel, Space–time VMS computation of wind-turbine rotor and tower aerodynamics, *Comput. Mech.* **53** (2014) 1–15.
100. K. Takizawa, T. E. Tezduyar, H. Mochizuki, H. Hattori, S. Mei, L. Pan and K. Montel, Space–time VMS method for flow computations with slip interfaces (ST-SI), *Math. Models Methods Appl. Sci.* **25** (2015) 2377–2406.
101. K. Takizawa, T. E. Tezduyar and Y. Otoguro, Stabilization and discontinuity-capturing parameters for space–time flow computations with finite element and isogeometric discretizations, *Comput. Mech.* **62** (2018) 1169–1186.
102. K. Takizawa, T. E. Tezduyar and T. Sasaki, Aorta modeling with the element-based zero-stress state and isogeometric discretization, *Comput. Mech.* **59** (2017) 265–280.
103. K. Takizawa, T. E. Tezduyar and T. Sasaki, Isogeometric hyperelastic shell analysis with out-of-plane deformation mapping, *Comput. Mech.* **63** (2019) 681–700.
104. K. Takizawa, T. E. Tezduyar and T. Terahara, Ram-air parachute structural and fluid mechanics computations with the space–time isogeometric analysis (ST-IGA). *Comput. Fluids* **141** (2016) 191–200.
105. K. Takizawa, T. E. Tezduyar, T. Terahara and T. Sasaki, Heart valve flow computation with the Space–Time Slip Interface Topology Change (ST-SI-TC) method and Isogeometric Analysis (IGA), in *Biomedical Technology: Modeling, Experiments and Simulation*, eds. P. Wriggers and T. Lenarz, Lecture Notes in Applied and Computational Mechanics (Springer, 2018), pp. 77–99.
106. K. Takizawa, T. E. Tezduyar, H. Uchikawa, T. Terahara, T. Sasaki and A. Yoshida, Mesh refinement influence and cardiac-cycle flow periodicity in aorta flow analysis with isogeometric discretization, *Comput. Fluids* **179** (2019) 790–798.
107. T. Terahara, T. Kuraishi, K. Takizawa and T. E. Tezduyar, Computational flow analysis with boundary layer and contact representation: II. Heart valve flow with leaflet contact, *J. Mech.* **38** (2022) 185–194.
108. T. Terahara, K. Takizawa, T. E. Tezduyar, Y. Bazilevs and M.-C. Hsu, Heart valve isogeometric sequentially-coupled FSI analysis with the space–time topology change method, *Comput. Mech.* **65** (2020) 1167–1187.
109. T. Terahara, K. Takizawa, T. E. Tezduyar, A. Tsushima and K. Shiozaki, Ventricle-valve-aorta flow analysis with the space–time isogeometric discretization and topology change, *Comput. Mech.* **65** (2020) 1343–1363.
110. T. E. Tezduyar, Stabilized finite element formulations for incompressible flow computations, *Adv. Appl. Mech.* **28** (1992) 1–44.

111. Y. Ueda, Y. Otoguro, K. Takizawa and T. E. Tezduyar, Element-splitting-invariant local-length-scale calculation in B-spline meshes for complex geometries, *Math. Models Methods Appl. Sci.* **30** (2020) 2139–2174.
112. T. M. van Opstal, J. Yan, C. Coley, J. A. Evans, T. Kvamsdal and Y. Bazilevs, Isogeometric divergence-conforming variational multiscale formulation of incompressible turbulent flows, *Comput. Methods Appl. Mech. Engrg.* **316** (2017) 859–879.
113. A. Vié, H. Pouransari, R. Zamansky and A. Mani, Particle-laden flows forced by the disperse phase: Comparison between Lagrangian and Eulerian simulations, *Int. J. Multiph. Flow* **79** (2016) 144–158.
114. B. Vreman, B. Geurts, N. Deen, J. Kuipers and J. Kuerten, Two-and four-way coupled Euler–Lagrangian large-eddy simulation of turbulent particle-laden channel flow, *Flow Turbul. Combust.* **82** (2009) 47–71.
115. S. Xu, N. Liu and J. Yan, Residual-based variational multi-scale modeling for particle-laden gravity currents over flat and triangular wavy terrains, *Comput. Fluids* **188** (2019) 114–124.
116. F. Xu, G. Moutsanidis, D. Kamensky, M.-C. Hsu, M. Murugan, A. Ghoshal and Y. Bazilevs, Compressible flows on moving domains: Stabilized methods, weakly enforced essential boundary conditions, sliding interfaces, and application to gas-turbine modeling, *Comput. Fluids* **158** (2017) 201–220.
117. J. Yan, X. Deng, A. Korobenko and Y. Bazilevs, Free-surface flow modeling and simulation of horizontal-axis tidal-stream turbines, *Comput. Fluids* **158** (2017) 157–166.
118. J. Yan, X. Deng, F. Xu, S. Xu and Q. Zhu, Numerical simulations of two back-to-back horizontal axis tidal stream turbines in free-surface flows, *J. Appl. Mech.* **87** (2020) 061001.
119. J. Yan, A. Korobenko, X. Deng and Y. Bazilevs, Computational free-surface fluid–structure interaction with application to floating offshore wind turbines, *Comput. Fluids* **141** (2016) 155–174.
120. J. Yan, A. Korobenko, A. E. Tejada-Martinez, R. Golshan and Y. Bazilevs, A new variational multiscale formulation for stratified incompressible turbulent flows, *Comput. Fluids* **158** (2017) 150–156.
121. J. Yan, S S. Lin, Y. Bazilevs and G. Wagner, Isogeometric analysis of multi-phase flows with surface tension and with application to dynamics of rising bubbles, *Comput. Fluids* **179** (2019) 777–789.
122. Y. Yu, Y. J. Zhang, K. Takizawa, T. E. Tezduyar and T. Sasaki, Anatomically realistic lumen motion representation in patient-specific space–time isogeometric flow analysis of coronary arteries with time-dependent medical-image data, *Comput. Mech.* **65** (2020) 395–404.
123. Q. Zhu and J. Yan, A moving-domain CFD solver in FEniCS with applications to tidal turbine simulations in turbulent flows, *Comput. Math. Appl.* **81** (2021) 532–546.
124. Q. Zhu, J. Yan, A. Tejada-Martínez and Y. Bazilevs, Variational multiscale modeling of Langmuir turbulent boundary layers in shallow water using isogeometric analysis, *Mech. Res. Comm.* **108** (2020) 103570.